Journal of the Australian Ceramic Society (2018) 54:357–368
https://doi.org/10.1007/s41779-017-0160-5

RESEARCH

Structural, magnetic, and electrical properties of Gd-substituted $LaFeO_3$ prepared by co-precipitation method

L. M. Salah[1] · M. Haroun[1] · M. M. Rashad[2]

Received: 6 April 2017 / Revised: 19 August 2017 / Accepted: 21 November 2017 / Published online: 28 November 2017
© Australian Ceramic Society 2017

Abstract
Gd-substituted $LaFeO_3$ polycrystalline samples were prepared by the co-precipitation method. A detailed investigation of the structural, magnetic, and electrical properties of the $La_{1-x}Gd_xFeO_3$ system was performed. The differences of the ionic radius and the electron configuration between Gd and La cause the distortion of the crystal structure. We have related it to the development of the magnetic and electrical properties. In addition, we provide the effect of the microstructure. The systematic variation of the octahedral-site tilting have been deduced by XRD, IR, and magnetic properties.

Keywords Perovskite · XRD · IR · Hysteresis loop · AC electrical properties

Introduction

$LaFeO_3$ with a typical ABO_3-type perovskite structure has gained great attention due to its broad applications in catalysis [1], chemical sensoring [2], and magnetic materials [3–5], and as an electrode in fuel cells [6] due to its ability to exhibit ferroelectric and ferromagnetic properties [7]. In this regard, many researchers attempt to improve its magnetic property by the replacement of La with different rare earth ions R [7–10]. This replacement induced the distortion of the structure and the reduction of the particle size [10].

The distortions of the perovskite structure with respect to the ideally cubic stable perovskite [11, 12] can be estimated by calculating the tolerance factor (t), $t = (r_A + r_O)/\sqrt{2}\,(r_B + r_O)$. Here, r_A and r_B are the cation radii with nine and six coordination numbers, respectively, and $r_O = 0.138$ nm is the oxygen anion radius in sixfold coordination [13]. The condition $t < 1$ is realized by cooperative rotations of the $BO_6/2$ octahedra that vary the B–O–B bond angle (φ) to be less than 180°. This angle can be modified by isovalent chemical substitutions on the A sites of ions of different ionic radii. Smaller A-site cations reduce to give a smaller bond angle φ. When this angle reduces, the orbital overlap integral over the B–O–B bonding array is therefore reduced by a factor of $\cos\varphi$ [14]. Zhou and Goodenough [14] have studied the development of the octahedral-site distortion as a function of ionic radius in $RFeO_3$ systems, and they found that the octahedral-site distortion is intrinsic to orthorhombic perovskites and is strongly bias orbital ordering and spin ordering in compounds that have the same structure. They conclude that the maximum octahedral-site distortion is at an intermediate ionic radius like that of Gd^{3+} ion, i.e., the maximum octahedral-site distortion is due to $GdFeO_3$ and the minimum is due to La FeO_3.

The magnetic ordering of the iron ions in both $LaFeO_3$ and $GdFeO_3$ essentially yield an A-type antiferromagnet [15, 16]. Each Fe^{3+} ion is surrounded by six O^{2-} ions arranged in FeO_6 octahedra. The O^{2-} is the common apex of the two adjacent octahedral acting as a superexchange interaction bond. According to the Dzyaloshinskii–Moriya antisymmetric exchange mechanism [15, 16], each Fe^{3+} magnetic moment is arranged not totally antiparallel to the moments of all six nearest Fe^{3+} neighbors but normally canting at a small angle θ, where $\varphi = 180° - \theta$. This arrangement of Fe^{3+} magnetic moments leads to the occurrence of weak ferromagnetism in the orthoferrite.

The conductivity in ferrites occurs as a result of electron hopping between Fe^{3+} and Fe^{2+} ion states on the octahedral

✉ L. M. Salah
lobna@sci.cu.edu.eg

M. M. Rashad
mrashad@cmrdi.sci.eg

[1] Physics Department, Faculty of Science, Cairo University, Giza, Egypt

[2] Central Metallurgical Research and Development Institute, P.O. Box: 87, Helwan, Cairo, Egypt

sites. The FeO_6 octahedra which share corners infinitely in all three dimensions are building units of $RFeO_3$ compound. The *Fe–Fe* distance is short which facilitates electron hopping from Fe^{3+} to Fe^{2+} between octahedral sites in this system. This hopping may be according to the double potential well models. The hopping from site to site may extend throughout the bulk, the sites forming an interconnected network through which the charges may flow. Some jumps are easier because of the small distance between sites. Moreover, the easier jumps contribute to dielectric relaxation whereas the more difficult jumps contribute to conduction [17]. By increasing frequency, the conductivity increases as a result of the pumping force caused by the applied frequency which helps in transferring the charge carriers between the different conduction states.

The interrelation between the structural constraints and the magnetic properties of pure $LaFeO_3$ and $GdFeO_3$was investigated [18]. The synthesis of $La_{1-x}Gd_xFeO_3$ by the self-combustion method is studied recently in Ref. [19]. In this work, we study the preparation of $La_{1-x}Gd_xFeO3$ by the co-precipitation routes. We provide a detailed investigation of the structural and microstructure of $La_{1-x}Gd_xFeO_3$ by studying XRD, FTIR, and FESEM. We relate the octahedral-site distortion to the development of the complex magnetic interactions. In addition, we provided measurements of AC conductivity as well as the real and imaginary parts of the dielectric constant for the mentioned compound, as a function of temperature and frequency, to unravel the complex sequence of its magnetic and electrical properties.

Experimental details

Synthesis

The investigated samples $La_{1-x}Gd_xFeO_3$ ($0 \le x \le 1.0$) were prepared by co-precipitation routes. Initial ingredients of metal nitrate were of high purity (BDH) and were taken in stoichiometric proportion. The co-precipitating agent was sodium hydroxide aqueous solution. The pH value was adjusted to 10 to ensure the formation of complete precipitation. The precipitate was washed with distilled water many times to remove the residual base. Then the precipitate was filtered and allowed to dry in a muffle furnace at 80 °C. All the prepared powders were calcined at 400 to 1200 °C for 2–4 h at a heating rate of 4 °C/min. The samples were fired using Lenton furnace UAF 16/5 (England). The prepared samples were checked by the X-ray diffraction to insure the formation of the required chemical formula. It was found that this method was adequate to prepare all concentrations of the chemical formula $La_{1-x}Gd_xFeO_3$ ($0 \le x \le 1.0$) with the heat treatment as follows: $x = 0.0$ and 1.0 at1200 for 2 h and $x = 0.2$–0.8 at 1000 °C for 4 h.

Sample characterization

X-ray diffraction patterns were obtained for all samples using Brucker Weis D8 diffractometer and Cu-Kα ($\lambda = 1.5406$ Å) radiation to assure that the structure of those samples is formed. The powder diffraction patterns were scanned at a step of 0.1° and step time 1 s. The average crystallite size was estimated using Scherrer's relationship after applying the correction for instrumental broadening [20].

FTIR spectra were recorded in air at room temperature with FTIR spectrometer (Spectrometer JASCO, 6300, Japan) over the range (150–650 cm^{-1}) with deuterated triglycine sulfate (DTGS) polyethylene window detector and over the range (1000–400 cm^{-1}) (using DTGS KBr windows detector). The transmission spectra were obtained on 1 mg of powdered sample dispersed in 98 mg of *KBr* pellet pressed under vacuum with the estimated error of ± 4 cm^{-1}.

Field emission scanning electron microscope images of products were imaged with QUANTA FEG250 (Netherlands).

The room temperature magnetic hysteresis of the samples was traced using vibrating sample magnetometer (Lake Shore 7410, USA).

The ac conductivity as well as the dielectric measurements of the samples under investigation were carried out from room temperature up to 850 K at frequencies ranging from 1 kHz to 5 MHz using LCR Hi Tester (HIOKI model 3531Z Japan). The sample was inserted between the two cell electrodes. The temperature of the sample was measured using T-type thermocouple connected to temperature controller with the junction in contact with the sample to avoid any temperature gradient.

Results and discussion

XRD analysis

The values of the tolerance factor are calculated and tabulated in Table 1. From this table, it is clear that $GdFeO_3$ is more distorted than the parent compound, i.e., with increasing cation substitution, the value of the tolerance factor deviates far from the ideal value and the degree of distortion systematically increases with increasing Gd content.

Table 1 Tolerance factor (t) of the structure $La_{1-x}Gd_xFeO_3$; $0.0 \le x \le 1.0$

x	0.0	0.2	0.4	0.6	0.8	1.0
t	0.9024	0.8949	0.8873	0.8797	0.8721	0.8645

Figure 1 shows X-ray diffraction patterns for $La_{1-x}Gd_xFeO_3$ ($0.0 \le x \le 1.0$). The preliminary investigation analysis of the patterns shows that the diffraction line of $La_{1-x}Gd_xFeO_3$ ($0 \le x \le 0.4$) is well indexed with (74-2263) JCPDS card number with the space group Pbnm (62), while $La_{1-x}Gd_xFeO_3$ ($0.6 \le x \le 1.0$) are completely matched with JCPDS card number (00-047-0067) with the same space group (62). Hexagonal phase of La_2O_3 and $Gd_3Fe_2Fe_3O_{12}$ is detected as a minor secondary phase for the concentration $x = 0.0$ and 0.8 respectively. The diffraction patterns show a slight shift in the peak position toward higher 2θ and the appearance of a number of planes with increasing Gd concentration. This suggests that progressive substitution of La^{3+} ions by Gd^{3+} leads to the contraction of the unit cell of $LaFeO_3$. This is related to the difference in ionic radii between Gd^{3+} (1.03 Å) and La^{3+} (1.16 Å). The appearance of a number of planes as Gd^{3+} ions increase can be explained by the fact that the atomic scattering factor of the Gd_{64} is larger than that of La_{57} [21].

The cell parameters a, b, and c and the unit cell volume are calculated according to one card (no. 00-047-0067) and tabulated in Table 2. Obviously, from Table 2, the lattice constants a and c are slightly decreasing, while b increases continuously on increasing Gd concentration. One can calculate the cell distortion d (the departure from the ideal cubic cell) given by the following equation: $d = [[((a/\sqrt{2}) - a_p)^2 + ((b/\sqrt{2}) - a_p)^2 + (c/2 - a_p)^2] \times 10^4]/3a_p^2$ [22], where a_p is the lattice parameter of the ideal cubic perovskite calculated from the equation $a_p = (a/\sqrt{2} + b/\sqrt{2} + c/2)/3$. The variation of the cell distortion factor versus the concentration of the substituted Gd^{3+} is represented in Table 2. The cell distortion factor increases with increasing the Gd^{3+}substitution. Such experimental results agree with the calculated values of the tolerance factor.

From Table 2, one can observe that a and b parameters are diverging with increasing the Gd^{3+} ion substitution. This divergence can be expressed by calculating the spontaneous orthorhombic strain (s) which is given by the following formula: $s = 2 \times (b - a)/(b + a)$ [23].The obtained results given in Table 2 confirm that the distortion is continuously increasing with Gd content. The increase of strain parameter s clearly indicates that the tilting of FeO_6 octahedra is increased and implies significant deviations of the Fe–O–Fe bond angle φ within the ab plane from 180°. However, the variation of the distortion determined from XRD patterns is systematic like the theoretical one.

Finally, the estimated average crystallite size using Scherrer's relationship with Gd concentration is presented in Fig. 2. It is clear from the figure that the highest value of the crystallite size is found to be $x = 0.0$ and 1.0. This can be attributed to the increase in the sintering temperature (1200 °C) for $x = 0.0$ and 1.0. It is well known that normally the increase in annealing temperature facilitates the grain growth. The crystallite sizes is found to decrease with increasing the Gd^{3+} ion up to 0.4. The results are as the previously mentioned in Refs. [8–10]. This is attributed to that the radius of Gd^{3+} (1.01 Å) is smaller than that of La^{3+} (1.16 Å) as the result of the shrinkage of unit cell. At higher ratio of Gd^{3+}, a clear increase of grain sizes is due to the fact that the Gd^{3+} ions accelerate the grain growth [24]. This fact is confirmed by the study similar to the previously published Ref. [19].

FTIR

The infrared spectra for $La_{1-x}Gd_xFeO_3$ ($0.0 \le x \le 1.0$) are shown in Fig. 3. The FTIR spectra that we obtain for compounds are quite similar to those reported elsewhere [18, 19].

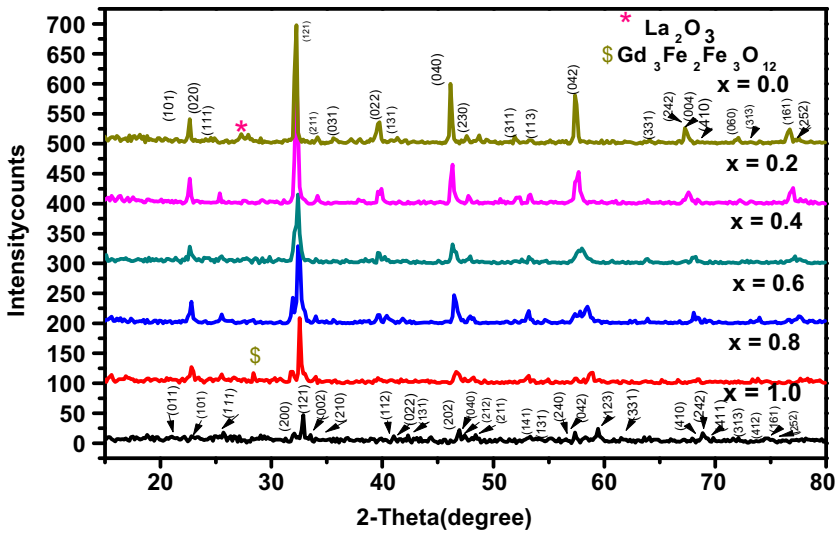

Fig. 1 XRD patterns of $La_{1-x}Gd_xFeO_3$ at different concentrations ($x = 0$, 0.2, 0.4, 0.6, 0.8, 1.0)

Table 2 Unit cell parameters, volume, cell distortion factor, and spontaneous orthorhombic strain of $La_{1-x}Gd_xFeO_3$

x	Unit cell parameters			Volume (Å)^3	Cell distortion factor	Spontaneous orthorhombic strain
	a (Å)	b (Å)	c (Å)			
0.0	5.5423	5.5587	7.8512	241.4	0.015	0.0030
0.2	5.4880	5.5621	7.8267	239.7	0.306	0.0134
0.4	5.4411	5.5640	7.8110	237.7	0.863	0.0224
0.6	5.3888	5.5850	7.7846	235.8	2.150	0.0358
0.8	5.3307	5.5960	7.7658	234.1	3.974	0.0486
1.0	5.3598	5.6012	7.6692	229.4	3.504	0.0441

By considering Fig. 3, one can identify three regions according to many references [25, 26]. The IR spectroscopic results are summarized in Table 3. The first region at the higher frequency, which is designated as $_s$ corresponds to the stretching mode which involves the internal motion of a change in length of the Fe–O bond in the FeO_6 octahedral. The second region lies in the range 500–200 cm^{-1} designated as $_b$ and corresponds to the bending mode which is sensitive to a change in the Fe–O–Fe bond angle in the FeO_6 octahedral. Several peaks are present in this region. As Gd increases (at $x = 1$), the phonon structures are broader and less resolved, probably due to increasing the disorder present in this sample. In addition, there is a shift of the $_b$ band to higher frequency as Gd concentration increases that reflects a decreasing of the bond length and angle of Fe–O–Fe. It indicates that the increasing of distortion of the Fe–O–Fe bond angle is observed as Gd cation increases. From Table 3, it is obvious that the increasing frequency for either $_s$ band or $_b$ band is not systematic. This result is confirmed by Fig. 4.

Generally, the prediction of increasing frequency for either band means that the force constant for such band increases. The increase of force constant is due to decrease of the bond length. This means that a change in length of the Fe–O bond in the FeO_6 octahedra is not systematically depending on concentration of Gd and is not related to the decrease in the lattice parameters with Gd content. The local lattice distortion however can modify the average lattice constant. The local changes of the bond angles and bond lengths are adjusted without involving large-scale diffusion of cations in the material. As is seen through the results of the lattice parameters coming from X-ray diffraction data, the changes result as a local adjustment of bond angles and bond lengths without involving large-scale diffusion of cations in the material, and it causes lattice volume shrinkage as the concentration of Gd increases [18, 27].

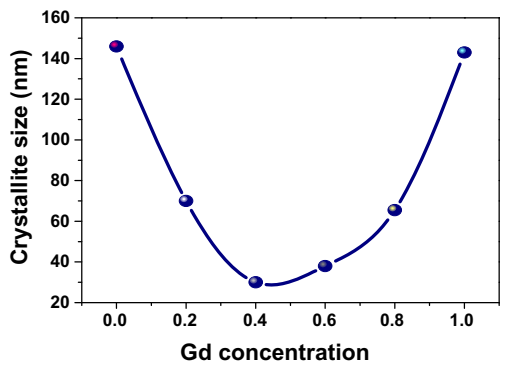

Fig. 2 Estimated crystallite size from XRD for $La_{1-x}Gd_xFeO_3$ ($x = 0$, 0.2, 0.4, 0.6, 0.8, 1.0) with the heat treatment as follows: $x = 0.0$ and 1.0 at 1200 °C for 2 h and $x = 0.2$–0.8 1000 °C for 4 h as a function in Gd concentration (x)

It is very important to mention that the major reason behind splitting (several peaks) of υ_b bands may be the strong electron–phonon interaction in all ferrites. This splitting was also observed in the same range for spinel structure in the ferrite materials [28, 29]. This may account for the nature of the octahedral site in the ferrite materials. The *Fe–Fe* distance is short in spinel and perovskite structure which facilitates electron hopping from Fe^{3+} to Fe^{2+} between octahedral sites. Hence, the activation energy for the hopping mechanism is less than the thermal energy at room temperature and the hopping process can be characterized by a hopping time $t_h = 3.5 \times 10^{-15}$ s at 300°K [30, 31]. Moreover, the interaction time in the IR absorption process is of the order of magnitude of hopping time.

The third region below 200 cm^{-1}which is designated as $_{ex}$ is the contribution of Fe–O bond of octahedral with lanthanides displacement [32].

However, the intensity ratio of $_s$ band to $_b$ band is found to reverse as the doping Gd ions increase. One can assume in a rough approximation that these changes are mainly due to variations in angles of the abovementioned rotations and to a lesser extent to changes in Fe–O distances. This observation was noticed by others [27]. It is clear that these three transmission spectra which are present in all investigated samples are much less broader and better resolved as La content increases probably due to decreasing the disorder present in this sample. This line broadening can make difficult or even impossible the experimental detection of some lines with small oscillator strength.

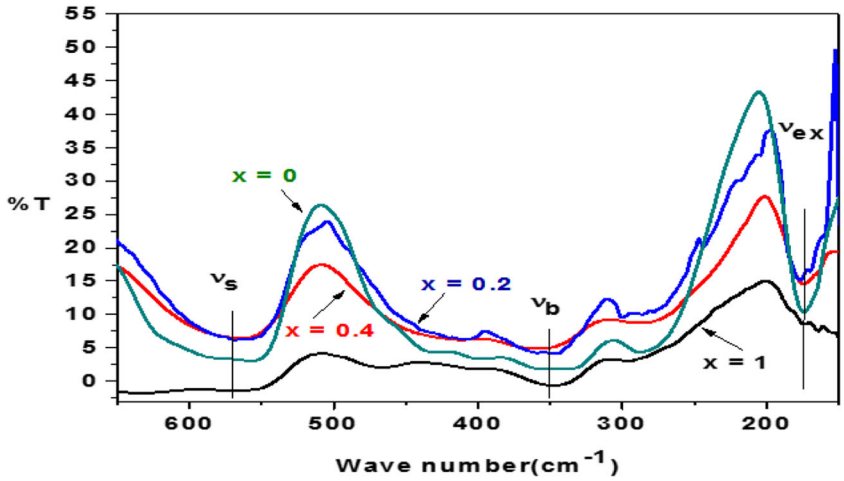

Fig. 3 Infrared transmission spectra of $La_{1-x}Gd_xFeO_3$ ($x = 0$, 0.2, 0.4, 1.0) in the range (650–150 cm^{-1}) (using DTGS polyethylene windows detector)

Finally, we conclude that the increase of distortion can be detected by the variation of the $_b$ band.

Microstructure

The surface morphology of $La_{1-x}Gd_xFeO_3$ ($x = 0.0$, 0.2, 0.4, 1.0) has been analyzed by FESEM images as given in Fig. 5. Evidently, the micrograph of $LaFeO_3$ particles shows agglomerated grains with different shapes and sizes as depicted in Fig. 5a. They exhibit non-uniform diameters and some particles appear as plate-like structure. The mean particle size of $LaFeO_3$ sample is estimated to be between 100 and 250 nm. The non-homogeneity of that sample can be arisen from intra-granular porosity (grain boundary pores), whereas intra-granular is mainly attributed to segregation of secondary phases toward grain boundaries. Therefore, the lack of secondary phases (3.5% of La_2O_3) through XRD patterns was considered as an evidence for the intra-granular pores type. However, the particle size for $x = (0.2, 0.4,$ and $1.0)$ tends to form rather homogeneous cluster aggregates. They exhibit regular shape morphology and uniform diameters. Apparently, the behavior of particle size of Gd-substituted $LaFeO_3$ samples are in good agreement with the calculated crystallite size given by XRD analysis, i.e., the lowest particle size is also observed for $x = 0.4$.

Magnetic properties

The room temperature M–H hysteresis loops of the prepared $La_{1-x}Gd_xFeO_3$ ($x = 0.0$, 0.2, 0.4, 0.6, and 1.0) are shown in Fig. 6. As shown from the figure, the hysteresis loops do not show a normal (s-shape) type of ferromagnetic behavior (except for $x = 0$), i.e., the hysteresis curves do not show saturation. Additionally, its total magnetization (M_s) is composed of two parts: paramagnetic component (linear contribution) and weak ferromagnetic component (loop). In this case, the spontaneous magnetization (M_s*) could be obtained by extrapolating the linear portion of the M–H curves to $H = 0$. The paramagnetic contribution is clearly increasing with paramagnetic ion (Gd: $4f^7$, spin only, $s = 7/2$) doping to the substitution of diamagnetic ions (La: $4f^0$, spin only, $s = 0$) and the weak ferromagnetic is slightly decreasing.

All the calculated and measured parameters for hysteresis loops are tabulated in Table 4. In this context, it is clear that the ferromagnetic contribution (M_s*) decreases as Gd^{3+} ions increase. As was mentioned before in X-ray analysis, the substituted ion of La^{3+} ions for Gd^{3+} ions will increase the strain and increase the tilting of the FeO_6 octahedral, which would lead to the decrease of Fe–O–Fe bond angle φ. Granted, the decrease of the in-plane a b, Fe–O–Fe bond angles from 180° (from 168.5° for $LaFeO_3$ to 147.8° for $GdFeO_3$) as determined from Rietveld analysis, and X-ray diffraction data [18] causes the decrease of its superexchange

Table 3 IR bands for $La_{1-x}Gd_xFeO_3$; $0.0 \le x \le 1.0$

x	υ_s (cm^{-1})	υ_b (cm^{-1})	υ_{ex} (cm^{-1})
0.0	620- 587- 557	436–398- 336- 288	174
0.2	568	405–361–345-299-286-278- 243- 216- 204	177–169- 160
0.4	565	411–355- 292	174
1.0	632–565	467–347- 295	173–163

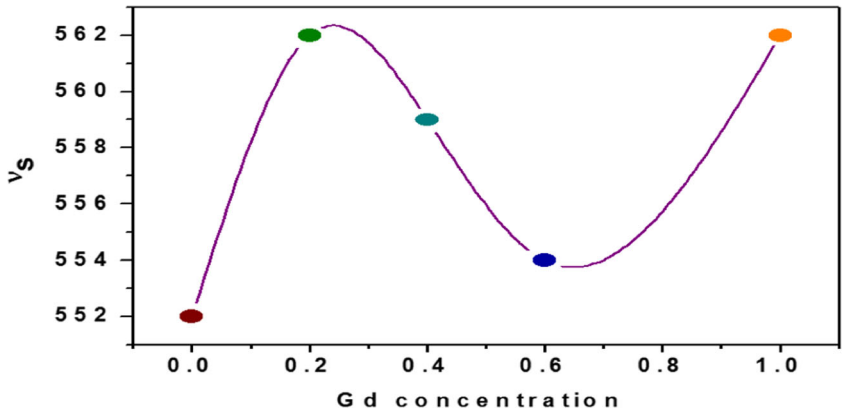

Fig. 4 Values of ν_s band at different concentration of Gd (values are taken from infrared transmission spectra in the range (1000–400 cm^{-1}) (using DTGS KBr windows detector)

interactions. As a consequence, the ferromagnetic contribution will be weakened but it will not alter the antiferromagnetic coupling along antiferromagnetic axis along c. This fact is clearly confirmed by the linear evolution of the loops from $LaFeO_3$ to $GdFeO_3$. Any other Fe–Fe coupling is very much smaller [33]. The fact that magnetic couplings of the type Fe–Gd and Gd–Gd are at least two orders of magnitude below the Fe–Fe coupling is also confirmed.

The coercive field has been noticed in the range of 48–880 Oe. From a closer look at Table 4, one can find that the coercive field H_c has the same trend with total magnetization (M_s) except for $LaFeO_3$. The values of H_c refer to the strength of the magnetic field required to reduce the magnetization of the magnetic sample to zero after the saturation magnetization has been reached. A large value of H_c for $LaFeO_3$ could be attributed to the increase of intra-granular porosity due to the

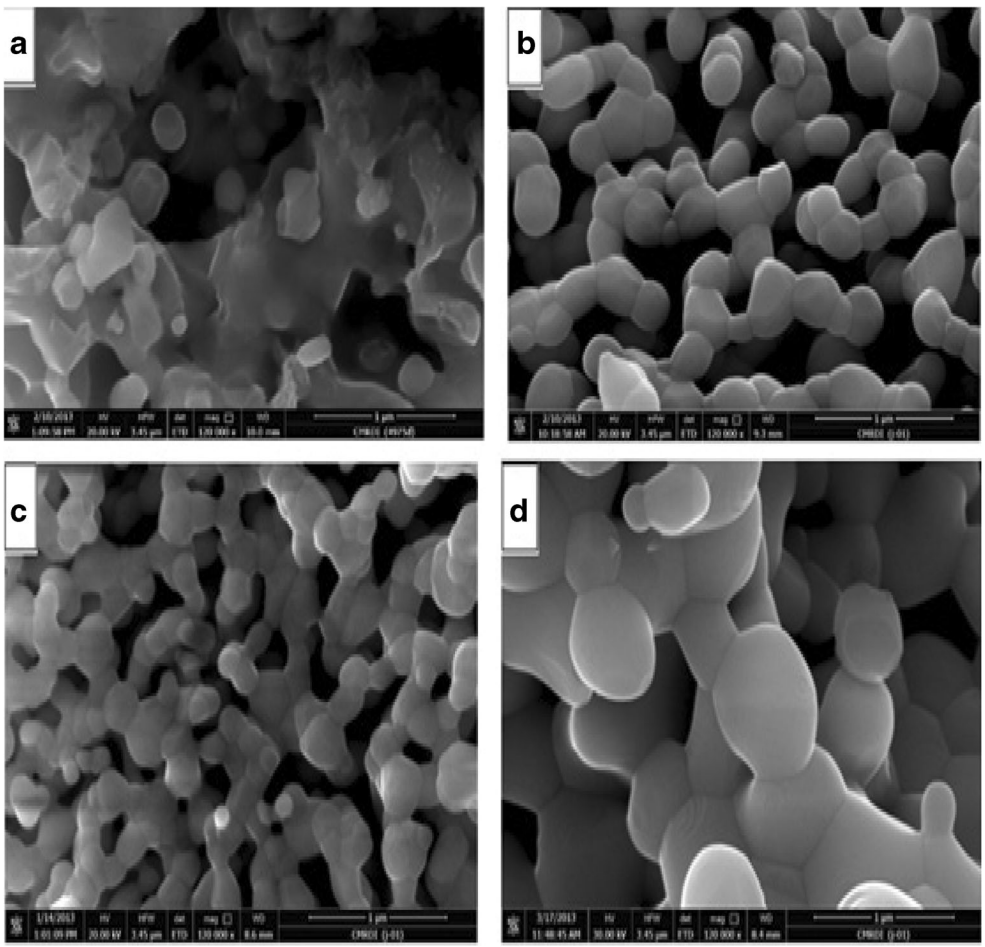

Fig. 5 FESEM of $La_{1-x}Gd_xFeO_3$ **a** $x = 0.0$, **b** $x = 0.2$, **c** $x = 0.4$, **d** $x = 1.0$ for the scale 1 μm

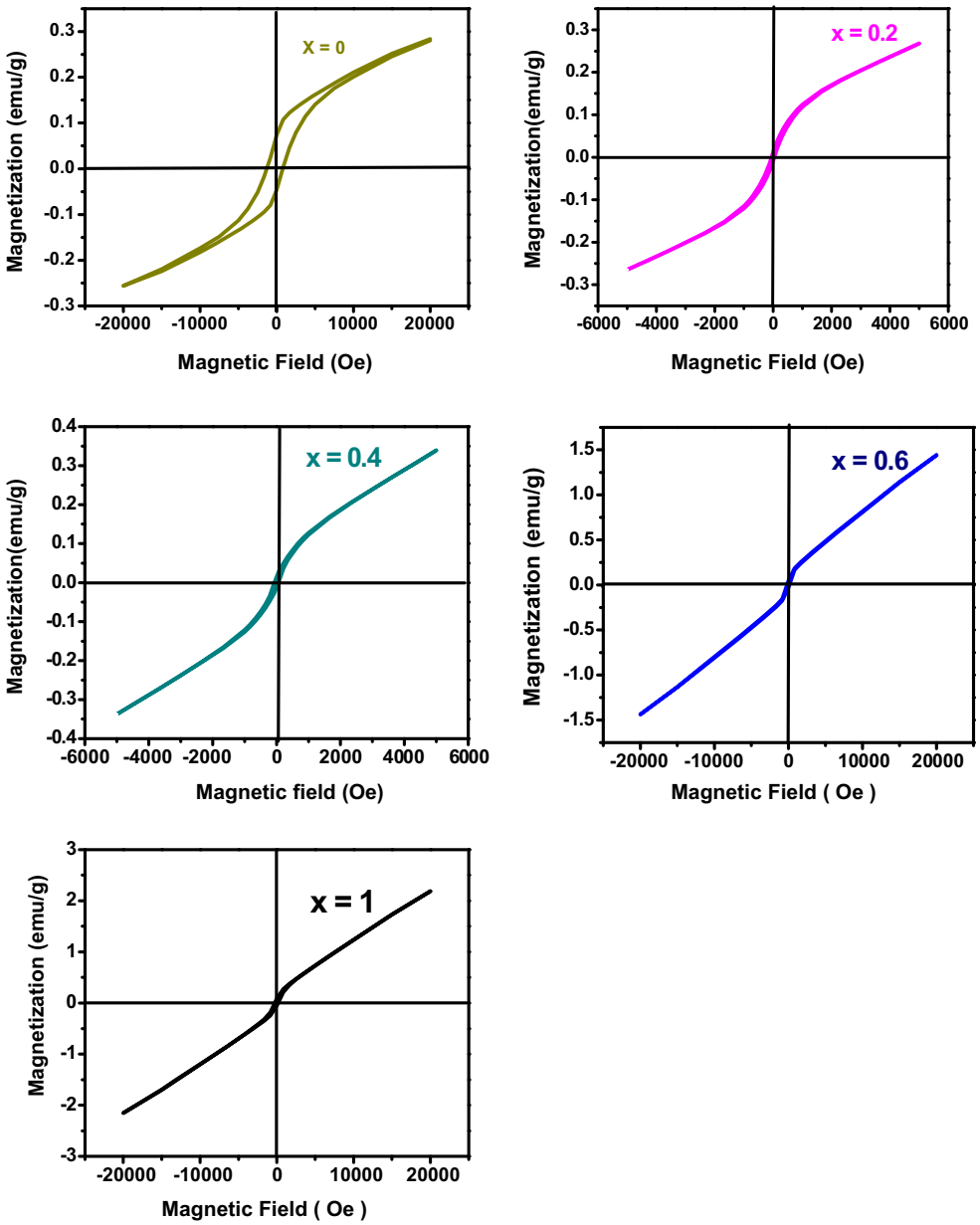

Fig. 6 M–H hysteresis loops of the $La_{1-x}Gd_xFeO_3$ samples prepared by co-precipitation method at different concentrations ($x = 0, 0.2, 0.4, 0.6, 1.0$)

secondary phase. The porosity has an important role in magnetization process because the pores work as a generator of a demagnetization field [34]. As the porosity increases, a higher field is needed to push the domain wall. On the other hand, the

Table 4 Magnetic parameters for $La_{1-x}Gd_xFeO_3$; $x = 0, 0.2, 0.4, 0.6, 1.0$

x	M_s (emu/g)	M_s* (emu/g)	M_r (emu/g)	H_c (Oe)	Crystallite size (nm)
0.0	0.30	0.130	70.6E-3	833.0	146
0.2	0.27	0.100	10.7E-3	48.2	70
0.4	0.33	0.080	13.7E-3	66.7	30
0.6	1.44	0.024	35.6E-3	150.3	38
1.0	2.17	0.03	69.6E-3	216.8	143

M_s is composed of two parts: paramagnetic component (linear contribution) and weak ferromagnetic component (loops)

M_s*which was obtained by extrapolating the linear portion of the M–H curves to $H = 0$

average particle size of this sample is also large. This can be understood by the fact that as the particle contains many grains, the magneto crystalline anisotropy is averaged over many grains and various orientation. The large anisotropy leads to an increase in coercivity with increasing particle size [35].

From Table 4, it is observed that the remanence M_r is in the range (10–70 emu/g). The remanence M_r also has the same tend with total magnetization (M_s) except for $LaFeO_3$ and $GdFeO_3$. The large value of remanence M_r for $LaFeO_3$ and $GdFeO_3$ could be attributed to the effect inter-granular porosity (pores trapped within the grains). Inter-granular porosity is directly proportional to the grain size growth which arises mainly from the increasing of the temperature of the annealing process.

Electrical properties

Figure 7 depicts the change of AC conductivity ln (σ) with the reciprocal of the absolute temperature as a function of frequency ranging from 1 kHz to 5 MHz for $La_{1-x}Gd_xFeO_3$ ($x = 0$, 0.2, 0.4, 1). It is clear that the trend of ln (σ) versus 1000/T for all investigated samples is nearly the same. Ordinarily in ferrite material, the increase in conductivity with increasing temperature may be related to the increase in the drift mobility of the charge carriers, which are localized at ions or vacant sites. From Fig. 7a–d, one can distinguish three different behavior of ln (σ) versus 1000/T which are denoted by regions (I), (II), and (III). In region (I), a frequency-dependent and nearly temperature-independent conductivity is observed. This is associated with a very small frequency-independent activation energy, reflecting an extrinsic type of conduction [36]. This means that starting with small thermal energy given to the system can liberate small number of the localized charges. At higher temperatures, region (II), the conductivity is frequency and temperature dependent, with a large frequency-dependent activation energy. It is noticed for the first part of this region that the conductivity decreases with increasing temperature; this decrease is a function of the frequency. This is due to the presence of trap centers of charges at the grain boundaries which are highly defected areas and act as scattering center for the flow of electrons. Therefore, grain boundaries are highly resistive [37]. Region (III) is characterized by an Arrhenius type behavior but with different slopes, which is a normal characteristic of semiconductor ferrites. At the end of this region, the conductivity is frequency independent.

From the figure, it is noticed that the largest value of lnσ is due to the concentration $x = 0.4$ up to certain temperature which is different for different frequencies. Then, a decrease in lnσ is observed beyond this temperature until reached to the smallest values of all concentrations. This indicates that the conduction mechanism at high temperatures is different from that at low temperatures. It should be remembered that the $x =$

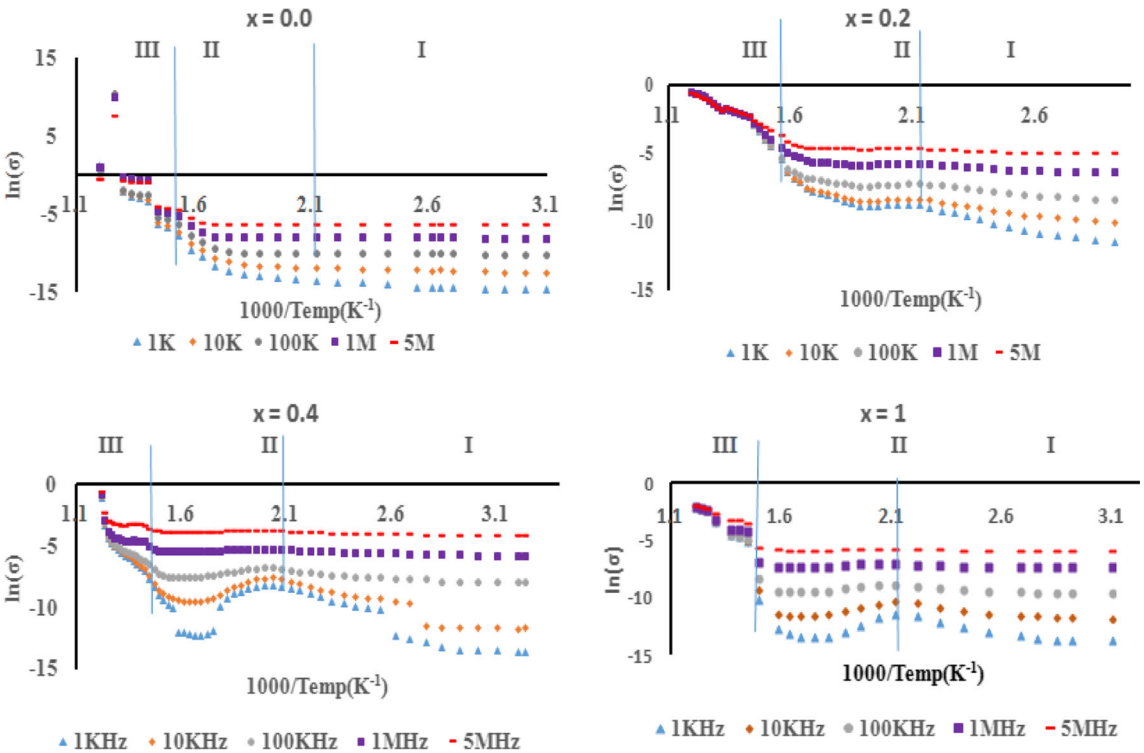

Fig. 7 AC conductivity ln (σ) versus the reciprocal of the absolute temperature as a function of frequency ranging from 1 kHz to 5 MHz for $La_{1-x}Gd_xFeO_3$ $x = 0$, 0.2, 0.4, 1

Table 5 Activation energy of $La_{1-x}Gd_xFeO_3$ ($x = 0$, 0.2, 0.4, 1.0) at 1 KHz frequency

x	0.0	0.2	0.4	1.0
Activation energy (eV)	1.23	0.59	1.04	1.42

0.4 has the smallest crystallite size of all concentrations. It is important to mention that the number of Fe^{3+} in octahedra is constant for all concentrations.

The activation energies calculated from the slope of ln (σ) versus 1000/T are listed in Table 5. It is seen from the table that the values of the activation energy are not systematically depending on concentration of Gd and they are not related to decrease in the lattice parameters with Gd content. In general, the value of the activation energy is related to the barrier height encountered by the hopping electron (inter-ionic distances in FeO_6 octahedra). That means that the decrease in the value of the lattice parameters with increasing Gd is not related to the systematic decrease of the inter-ionic distances in perovskite structure. This is in good agreement with IR analysis data. However, the energy barriers are of the order of 0.59–1.42 eV.

It is noted that for $LaFeO_3$ system, the conductivity σ shows an abrupt jump toward high temperature at $T \cong 833$ K. This is attributed to change in phase transition which is reported in accordance with the cooperative Jahn–Teller [38] or orbital-ordering transition [14, 39]. The same anomaly was seen for $LaMnO_3$ at $T \cong 747$ K [39] and at $T \cong 1100$ K for $PrMnO_3$ [40]. The authors have reported that with decreasing ionic radius of rare earth, the anomaly in σ, i.e., transition temperature, is shifted toward higher T until Nd. But, with smaller r_a than r_{Nd}, no such anomaly was observed up to 1500 K. They concluded that the orbital-ordering state is extremely stable with small r_a. This may explain that we do not observe this transition temperature for $GdFeO_3$.

Figure 8 shows the real part of dielectric constant (ε') for $La_{1-x}Gd_xFeO_3$ ($x = 0.0$, 0.2, 0.4, 1) as a function of the applied frequency ranging from 1 kHz to 5 MHz. From this figure, it is clear that the general trend at all frequencies is appearance of two peaks at two different ranges of temperatures. Obviously, the values of these peaks are decreasing rapidly as the frequency is increasing. Otherwise, the dielectric constant (ε') is almost small and independent of the temperature and frequency in the first temperature region and the range between the two peaks. The polarization phenomenon explains directly the behavior dielectric of materials. Polarization mechanism of

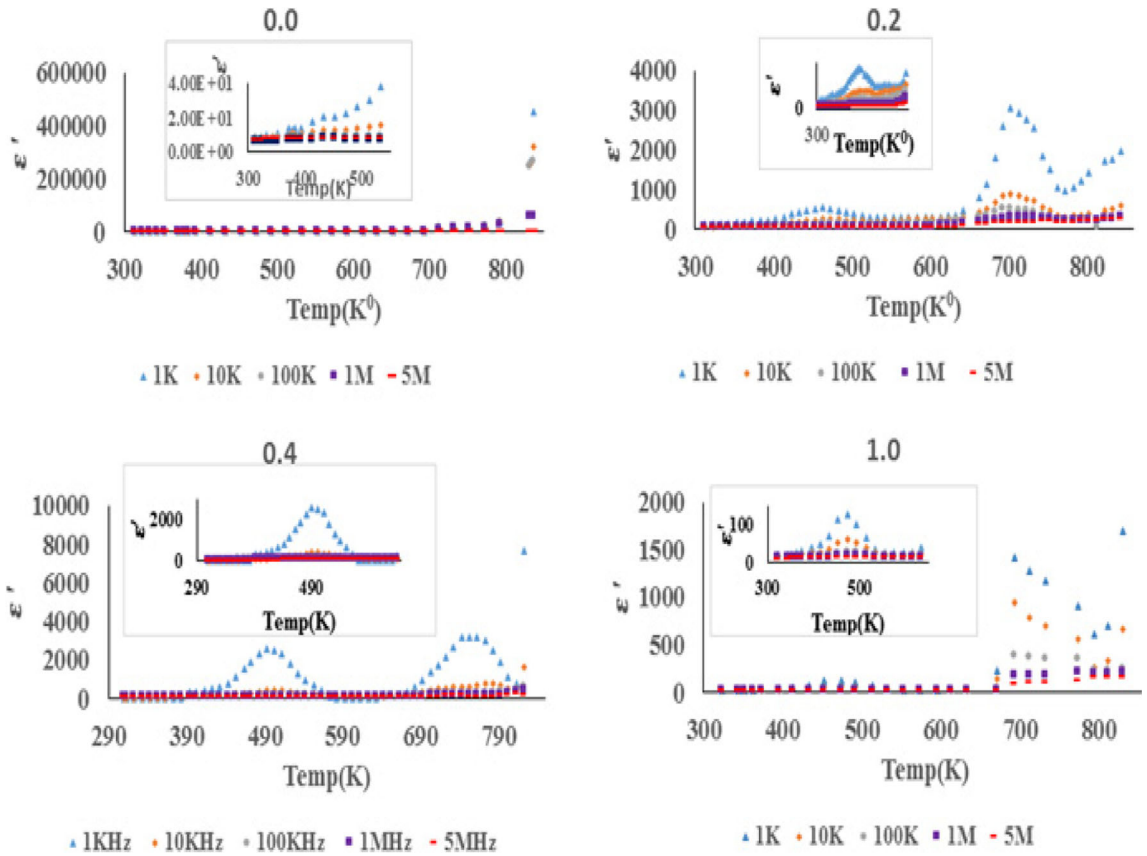

Fig. 8 Dielectric constant (ε') for $La_{1-x}Gd_xFeO_3$; ($x = 0.0$, 0.2, 0.4, 1.0) as a function of the applied frequency ranging from 1 kHz to 5 MHz (inset: to clarify the frequency dependence of the peak near 500 K)

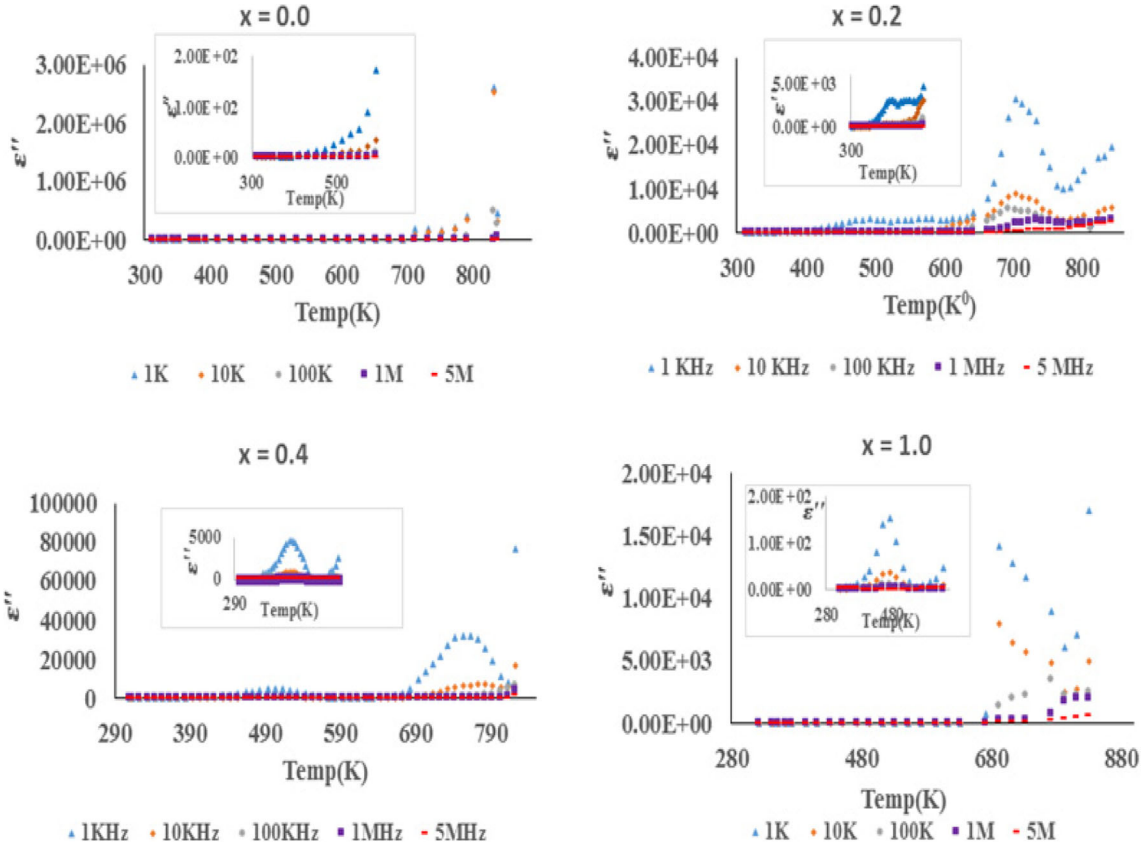

Fig. 9 Dielectric loss factor (ε'') for $La_{1-x}Gd_xFeO_3$ at different concentrations ($x = 0.0, 0.2, 0.4, 1.0$) as a function of the applied frequency ranging from 1 kHz to 5 MHz (inset: to clarify the frequency dependence of the peak near 500 K)

ferrites often occurs in a similar way to conductivity mechanism [41]. An applied external electric field causes a polarization by displacing electrons with electronic exchange ($Fe^{2+} \leftrightarrow Fe^{3+} + e^{-}$). To characterize the rapid decrease of dielectric constant at sufficiently low frequencies [42], we take Maxwell–Wagner model as a basis. According to Maxwell–Wagner model, high dielectric constant is due to the polarization of surface charges. High polarization is due to non-homogeneous structure of the sample. The dielectric structure of the sample consists of conducting grains and poorly conducting grain boundary. Variation of conductivity in the interface between these regions results in an accumulation of charges in the grain boundaries. As frequency rises, the charges cannot follow applied external field and consequently cannot contribute to polarization [43]. As a result, the dielectric constant becomes smaller after surface charge contribution loses its effect and gets eliminated [44, 45].

The temperature dependence of the dielectric loss factor (ε'') for $La_{1-x}Gd_xFeO_3$ at different concentrations ($x = 0.0$, 0.2, 0.4, 1) as a function of the applied frequency is shown in Fig. 9. From this figure, it is clear that the general behavior of the dielectric loss factor (ε'') for all samples at all frequencies with temperature is similar to that of dielectric constant (ε'). It can be stated that the sample exhibited two peaks corresponding to low-and high-temperature regions. Both peaks shift to higher temperatures as frequencies increase, as a sign that they are thermally activated. Consequently, each of relaxation times can be said to decrease with increasing temperature. Thus, the initial relaxation takes a long time, and the latter takes a short time to occur [46]. It is important to mention that for all ranges of the frequency (1 KHz–5 MHz), a peak of type Debye-like relaxation is not detectable. The relaxation may be partially masked due to the flow of the space charges through the conducting grains. However, AC measurements ($\ln\sigma$, ε',and ε'') for $La_{1-x}Gd_xFeO_3$ confirm the assumption that the mechanisms of the conductivity and the dielectric constant are of the same origin.

Conclusion

We have successfully synthesized polycrystalline samples of the single phase of the system $La_{1-x}Gd_xFeO_3$ of the most of the concentration range using the co-precipitating method. The concentration dependence of the lattice constants witnesses the increase of orthorhombicity via stronger tilting as a result of the decrease of the tolerance factor via the substitution of the larger La by the smaller Gd ions.

Far-infrared absorption reveals changes in phonon energy due to a decreasing of the Fe–O–Fe angle in FeO_6 octahedra units. Meanwhile, the change in length of the Fe–O bond in octahedral FeO_6 is not systematically depending on concentration of Gd and is not related to decrease in the lattice parameters with Gd content.

From the magnetization measurements of the doped compounds, we provide clear experimental evidence for an antiferromagnetic contribution of the magnetic ordering of the Fe moments. The weak ferromagnetic behavior decreases as Gd ions increase as a result of the decrease of the Fe–O–Fe superexchange bond angle caused by a distortion of the crystal structure. The large value of the coercive field and the remanence for some concentration are mainly due to microstructure effect.

Two peaks in ε' and ε'' with temperature dependence are detected. The dielectric constant is independent of frequency and temperature in the range beyond the relaxation frequency. Most interestingly, we observe a phase transition at 833 K for pure $LaFeO_3$.

Acknowledgements This research is financially supported by the Central Metallurgical Research and Development Institute, Egypt.

References

1. Wang, Y., Yang, X., Lu, L., Wang, X.: Experimental study on preparation of $LaMO_3$ (M = Fe, Co, Ni) nanocrystals and their catalytic activity. Thermochim Acta. **443**, 225–230 (2006)
2. Khetre, S.M., Chopade, A.U., Khilare, C.J., Kulal, S.R., Jadhav, H.V., Jagadale, P.N., Bangale, S.V., Bamane, S.R.: Ethanol gas sensing properties of nano-porous $LaFeO_3$ thick films. J of Shivaji Uni (Sci & Tech). **41**(2), 250–5347,**1-3** (2014)
3. Paul Blessington Selvadurai, A., Pazhanivelu, V., Jagadeeshwaran, C., Murugaraj, R., Panneer Muthuselvam, I., Chou, F.C.: Influence of Cr substitution on structural, magnetic and electrical conductivity spectra of $LaFeO_3$. J Alloys Compd. **646**, 924–931 (2015)
4. Phokha, S., Hunpratup, S., Pinitsoontorn, S., Putasaeng, B., Rujirawat, S., Maensiri, S.: Structure, magnetic, and dielectric properties of Ti-doped $LaFeO_3$ ceramics synthesized by polymer pyrolysis method. Mater Res B. **67**, 118–125 (2015)
5. Thirumalairajan, S., Girija, K., Mastelar, V.R., Ponpandian, N.: Investigation on magnetic and electric properties of morphologically different perovskite $LaFeO_3$ nanostructures. J Mater Sci Mater Electron. **26**, 8652–8662 (2015)
6. Hao Hung, M., Madhava Rao, M.V., Shyang Tsai, D.: Microstructures and electrical properties of calcium substituted $LaFeO_3$ as SOFC cathode. Mater Chem Phys. **101**, 297–302 (2007)
7. Acharya, S., Mondal, J., Ghosh, S., Roy, S.K., Chakrabarti, P.K.: Multiferroic behavior of lanthanum orthoferrite ($LaFeO_3$). MaterLett. **64**, 415–418 (2010)
8. Shikha, P., Kang, T.S., Randhawa, B.S.: Effect of different synthetic routes on the structural, morphological and magnetic properties of Ce doped $LaFeO_3$ nanoparticles. J Alloys Compd. **625**, 336–345 (2015)
9. Hosseini, S.A., Taghi, M., Sorkhani, S., Ahmadi, L.K., Alemi, A., Niaei, A., Salari, D.: Synthesis, characterization, and catalytic activity of nanocrystalline $La_{1-x}Eu_xFeO_3$ during the combustion of toluene. Chin J Catal. **32**, 1465–1468 (2011)
10. Ekaphan, S., Attaphol, K., Sumalin, P., Sitchai, H., Thanin, P.: Investigation of structural, morphological, optical, and magnetic properties of Sm-doped $LaFeO_3$ nanopowders prepared by sol–gel method. J Sol Gel Technol. **81**, 483–492 (2017). https://doi.org/10.1007/s10971-016-4212-z
11. Woodward, P.M.: Octahedral tilting in perovskites. I. Geometrical considerations. Acta Crystallogr Sect B: Struct Sci. **53**, 32–43 (1997)
12. Aleksandrov, K.S., Bartolome, J.: Structural distortions in families of perovskite-like crystals. Phase Transition. **74**, 255–335 (2001)
13. Shannon, R.D.: Revised effective ionic radii and systematic studies of interatomic distances in halides and chalcogenides. Acta Crystallogr. **A32**, 751–767 (1976)
14. Zhou, J.S., Goodenough, J.B.: Intrinsic structural distortion in orthorhombic perovskite oxides. Phys Rev B. **77**, 132104-1-4 (2008). https://doi.org/10.1103/PhysRevB.77.132104
15. Treves, D.: Studies on orthoferrites at the Weizmann Institute of Science. J Appl Phys. **36**, 1033–1039 (1965)
16. Seo, J.W., Fullerton, E.E., Nolting, F., Scholl, A., Fompeyrine, J., Locquet, J.P.: Antiferromagnetic LaFeO3 thin films and their effect on exchange bias. J Phys Condens Matter. **20**, 264014-1-10 (2008)
17. Raju, G.G.: Dielectric in electric fields. CRC press. (2003)
18. Romero, M., Gómez, R.W., Marquina, V., Pérez-Mazariego, J.L., Pérez-Mazariego, J.L., Escamilla, R.: Synthesis by molten salt method of the$AFeO_3$ system (A=La, Gd)and its structural, vibrational and internal hyperfine magnetic field characterization. Physica B. **443**, 90–94 (2014)
19. Wiglusz, R.J., Kordek, K., Małecka, M., Ciupa, A., Ptak, M., Pazik, R., Pohlc, P., Kaczorowskia, D.: A new approach in the synthesis of $La_{1-x}Gd_xFeO_3$perovskite nanoparticles – structural and magnetic characterization. The Royal Society of Chemistry (Dalton Trans). **44**, 20067–20074 (2015). https://doi.org/10.1039/c5dt03378k
20. Cullity, B.D.: Elements of X-ray diffraction. Adison-Wesley Publ. Co., London (1967)
21. Pecharsky, V.K., Zavalij, P. Y. : Fundamentals of powder diffraction and structural characterization of materials, Springer Science +Business Media, Inc. (2003)
22. Vasylechko, L., Akselrud, L., Matkovskii, A., Sugak, D., Durygin, A., Frukacz, Z.: Crystal structure of the compound $Y_{0.5}Er_{0.5}AlO_3$. J Alloys Compd. **242**, 18–21 (1996)
23. Ain, M., Delrieu, J.-M., Menelle, A., Parette, G., Jegoudez, J.: Orthorhombicity and oxygen uptake by $YBa_2Cu_3O_{6+x}$. J Phys France. **50**, 1455–1461 (1989)
24. Yuantao, N.: Influence of Gd addition on the structure and properties of Au-Ni and Au-Ni-Cr alloys. Gold Bull. **39/4**, 220–225 (2006)
25. Gao, F., Lewis, R.A., Wang, X.L., Dou, S.X.: Infrared absorption of lanthanum manganites. Physica C. **2235**, 341–348 (2000)
26. Paolone, A., Roy, P., Pimenov, A., Loidl, A., Mel'nikov, O.K., Shapiro, A.Y.: Infrared phonon spectrum of pure and doped $LaMnO_3$. Phys Rev. **61**(17), 11255–11258 (2000)
27. Wang, X., Cui, Q.L., Pan, Y.W., Gao, W., Zhang, J., Zou, G.T.: High pressure effects on the Jahn-Teller distortion in perovskite $La_{0.5-x}Bi_xCa_{0.5}MnO_3$. J Alloys Compd. **321**, 72–75 (2001)
28. Mazen, S.A., Mansour, S.F., Dhahri, E., Zaki, H.M., Elmosalami, T.A.: The infrared absorption and dielectric properties of Li–Ga ferrite. J Alloys Compd. **470**, 294–300 (2009)
29. Ivanovskaya, M.I., Tolstik, A.I., Kotsikau, D.A., Pankov, V.V.: The structural characteristics of Zn–Mn ferrite synthesized by spray pyrolysis. Russ J Phys Chem. **A83**(12), 2081–2086 (2009)
30. Salah, L.M.: Spectroscopic studies of the effect of addition of Y^{3+} on structural characteristics of Ni-Zn ferrites. Phys Stat Sol (a). **203**(2), 271–281 (2006). https://doi.org/10.1002/pssa.200521285
31. Gupta, R., Sood, A.K., Metecalf, P., Honig, J.M.: Raman study of stoichiometric and Zn-doped Fe3O4. Phys Rev. **65**, 104430-1-8 (2002)

32. Mathur, P., Thakur, A., Singh, M.: Effect of nanoparticles on the magnetic properties of Mn–Zn soft ferrite. J Magn Mater. **320**, 1364–1369 (2008)
33. Eibschutz, M., Shtrikman, S., Trevest, D.: Mössbauer studies of Fe_{57} in orthoferrites. Phys Rev. **156**(2), 562–577 (1967)
34. Jadhav, S.S., Shirsath, S.E., Patange, S.M., Jadhav, K.M.: Effect of Zn substitution on magnetic properties of nanocrystalline cobalt ferrite. J Appl Phys. **108**(093920), 1–6 (2010)
35. Diandra, L.L., Reuben, D.R.: Magnetic properties of nanostructured materials. Chem Mater. **8**, 1770–1783 (1996)
36. Mostafa, M.F., Montasser, S.S.: AC conduction mechanism in perovskite-like dimers$(C_2H_8NO)_2M_2X_6$, M=Co/Cu, X=Cl/Br. Z. Naturforsch. **55a**, 945–956 (2000)
37. Low, K.O., Sale, F.R.: Electromagnetic properties of gel-derived NiCuZn ferrites. J Magn Magn Mater. **246**, 30–35 (2002)
38. Hemberger, J., Lobina, S., Krug von Nidda, H.-A., Tristan, N., Ivanov, V.Y., Mukhin, A.A., Balbashov, A.M., Loid, A.: Complex interplay of 3d and 4f magnetism in $La_{1-x}Gd_xMnO_3$. Phys Rev B. **70**, 024414-70 1-8 (2004). https://doi.org/10.1103/PhysRevB.70.024414
39. Zhou J.-S.,, Goodenough, J.B. : Orbital order-disorder transition in single-valent manganites**.** Phys. Rev. B 68, (2003) https://doi.org/10.1103/PhysRevB.68.144406
40. Kimura, T., Ishihara, S., Shintani, H., Arima, T., Takahashi, K.T., Ishizaka, K., Tokura, Y.: Distorted perovskite with e^1_g configuration as a frustrated spin system. Phys Rev B. **68**, 060403-1-4 (2003)
41. Liu, J., Duan, C., Yin, W., Mei, W.N., Smith, R.W., Hard, J.: Large dielectric constant and Maxwell-Wagner relaxation in $Bi_{2/3}Cu_3Ti_4O_{12}$. Phys Rev B. **70**, 144106-1-7 (2004)
42. Abdeen, A.M.: Dielectric behaviour in Ni–Zn ferrites. J Magn Magn Mater. **192**, 121–129 (1999)
43. Elkestawy, M.A., Kader, S.E., Amer, M.A.: AC conductivity and dielectric properties of Ti-doped $CoCr_{1.2}Fe_{0.8}O_4$ spinel ferrite. Phys B. **405**, 619–624 (2010)
44. Patange, S.M., Shirsath, S.E., Lohar, K.S., Jadhav, S.S., Kulkarni, N., Jadhav, K.M.: Electrical and switching properties of $NiAl_xFe_{2-x}O_4$ ferrites synthesized by chemical method. Phys B : Condensed Matter. **406**, 663–668 (2011)
45. Farea, A.M.M., Kumar, S., Batoo, K.M., Yousef, A., Lee, C.G.A.: Structure and electrical properties of $Co_{0.5}Cd_xFe_{2.5-x}O_4$ ferrites. J Alloys Compd. **464**, 361–369 (2008)
46. Tan, M., Koseoglu, Y., Alan, F., Sentrurk, E.: Overlapping large polaron tunneling conductivity and giant dielectric constant in $Ni_{0.5}Zn_{0.5}Fe_{1.5}Cr_{0.5}O_4$ nanoparticles (NPs). J Alloys Compd. **509**, 9399–9405 (2011)